Ni^{3+}-induced semiconductor-to-metal transition in spinel nickel cobaltite thin films

X. C. Huang,[1,*] W.-W. Li,[2,*] S. Zhang,[3] F. E. Oropeza,[4] G. Gorni,[5] V. A. de la Peña-O'Shea,[4] T.-L. Lee,[6] M. Wu,[7] L.-S. Wang,[8] D.-C. Qi,[9] L. Qiao,[3,†] J. Cheng,[1,‡] and K. H. L. Zhang[1,§]

[1]*State Key Laboratory of Physical Chemistry of Solid Surfaces, College of Chemistry and Chemical Engineering, Xiamen University, Xiamen 361005, People's Republic of China*

[2]*MIIT Key Laboratory of Aerospace Information Materials and Physics, College of Science, Nanjing University of Aeronautics and Astronautics, Nanjing 211106, People's Republic of China*

[3]*School of Physics, University of Electronic Science and Technology of China, Chengdu 610054, People's Republic of China*

[4]*Photoactivated Processes Unit, IMDEA Energy Institute, Parque Tecnológico de Móstoles, Avda. Ramón de la Sagra 3, 28935 Móstoles, Madrid, Spain*

[5]*CELLS-ALBA Synchrotron, Carrer de la Llum 2-26, 08290 Cerdanyola del Vallès, Spain*

[6]*Diamond Light Source Ltd., Harwell Science and Innovation Campus, Didcot OX11 0DE, United Kingdom*

[7]*Department of Physics, Xiamen University, Xiamen, 361005, People's Republic of China*

[8]*Fujian Key Laboratory of Materials Genome, College of Materials, Xiamen University, Xiamen 361005, People's Republic of China*

[9]*School of Chemistry, Physics and Mechanical Engineering, Queensland University of Technology, Brisbane, Queensland 4001, Australia*

(Received 2 June 2021; revised 16 August 2021; accepted 8 September 2021; published 23 September 2021)

In this paper, we report insights into the local atomic and electronic structure of $NiCo_2O_4$ epitaxial thin films and its correlation with electrical, optical, and magnetic properties. We grew structurally well-defined $NiCo_2O_4$ epitaxial thin films with controlled properties on $MgAl_2O_4(001)$ substrates using pulsed laser deposition. Films grown at low temperatures (<400 °C) exhibit a ferrimagnetic and metallic behavior, while those grown at high temperatures are nonmagnetic semiconductors. The electronic structure and cation local atomic coordination of the respective films were investigated using a combination of resonant photoemission spectroscopy, x-ray absorption spectroscopy, and *ab initio* calculations. Our results unambiguously reveal that the Ni^{3+} valence state promoted at low growth temperature introduces delocalized Ni 3*d*-derived states at the Fermi level (E_F), responsible for the metallic state in $NiCo_2O_4$, while the Co 3*d*-related state is more localized at higher binding energy. In the semiconducting films, the valence state of Ni is lowered and $\sim +2$. Further structural and defect chemistry studies indicate that the formation of oxygen vacancies and secondary CoO phases at high growth temperature are responsible for the Ni^{2+} valence state in $NiCo_2O_4$. The Ni 3*d*-related state becomes localized away from E_F, opening a band gap for a semiconducting state. The band gap of the semiconducting $NiCo_2O_4$ is estimated to be <0.8 eV, which is much smaller than the quoted values in the literature ranging from 1.1 to 2.58 eV. Despite the small band gap, its optical transition is *d*-*d* dipole forbidden, and therefore, the semiconducting $NiCo_2O_4$ still shows reasonable transparency in the infrared-visible light region. The present insights into the role of Ni^{3+} in determining the electronic structure and defect chemistry of $NiCo_2O_4$ provide important guidance for use of $NiCo_2O_4$ in electrocatalysis and opto-electronics.

DOI: 10.1103/PhysRevB.104.125136

I. INTRODUCTION

Complex transition metal oxides (TMOs) display a rich variety of fascinating electronic, optical, and magnetic properties, holding great promise for various applications in opto-electronics, spintronics, and renewable energy technologies [1,2]. Among them, spinel nickel cobaltite ($NiCo_2O_4$) has been attracting considerable attention in recent years. $NiCo_2O_4$ possesses very high electrical conductivity and good transparency in the infrared light region, making it a promising electrode material for solar cells and flat panel displays [3–6]. $NiCo_2O_4$ also shows a ferrimagnetic property with a high Curie temperature (T_C) of 400 °C, of particular importance for developing oxide-based spintronic devices [7]. Furthermore, because of the rich redox chemistry provided by the mixed valence states of Ni and Co, $NiCo_2O_4$ is also being widely explored as an efficient energy material for uses such as electrocatalysts for water electrolysis, electrodes for supercapacitors, and Li ion batteries [8–13].

The multifunctional properties of $NiCo_2O_4$ are fundamentally determined by the cation distribution, valence states, and local coordination of Ni and Co. $NiCo_2O_4$ is generally considered to have an inverse spinel structure, with the tetrahedral (T_d) site occupied by Co and the octahedral (O_h) site equally populated by Ni and Co (see Fig. 1) [6,7,14,15]. In an ideal inverse spinel case, Co cations at the T_d site have a Co^{3+} state, Ni cations at O_h have a Ni^{2+} state, and Co cations at O_h have a Co^{3+} state, i.e., $[Co^{3+}]_{T_d}[Ni^{2+}Co^{3+}]_{O_h}O_4$. However, in many practical cases, it has been reported that, depending

*These authors contributed equally to this paper.
†liang.qiao@uestc.edu.cn
‡chengjun@xmu.edu.cn
§kelvinzhang@xmu.edu.cn

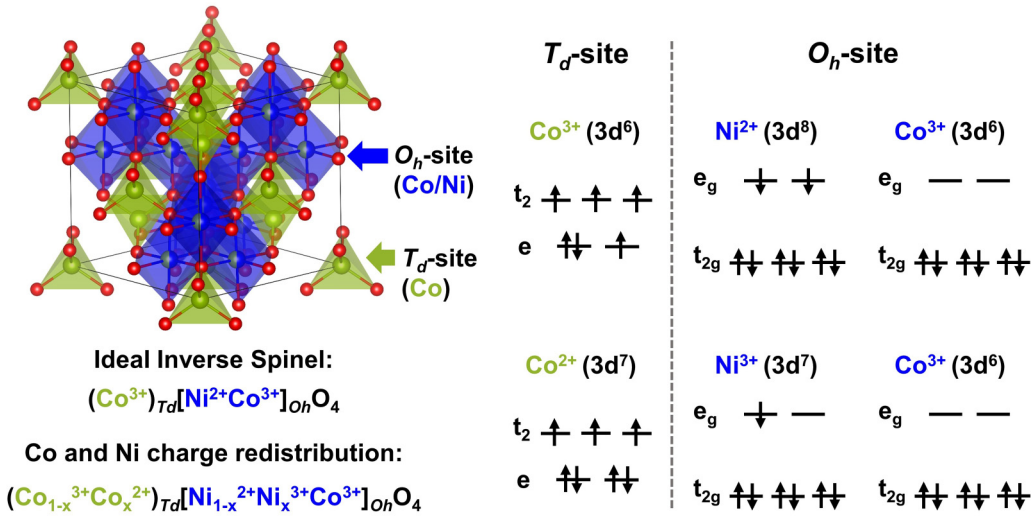

FIG. 1. Inverse spinel structure of $NiCo_2O_4$ (left) and spin occupations of the $3d$ states of Ni and Co ions in the inverse spinel structure (right).

on the material synthesis conditions, a certain amount of Co at the T_d site can be at a Co^{2+} state, which will push Ni at O_h to be at a $+3$ state, leading to a mixed valence state of $[Co^{3+}_{1-x}Co^{2+}_x]_{T_d}[Ni^{2+}_{1-x}Ni^{3+}_xCo^{3+}]_{O_h}O_4$ [16–18]. The mixed valence states of Co and Ni in both T_d and O_h coordination environments, together with other possible point defects such as antisite defects (e.g., Ni at the T_d site) or oxygen vacancies, lead to a range of different electronic configurations of the Ni $3d$ and Co $3d$ orbitals (Fig. 1) and thereby give rise to the abovementioned richness of properties of $NiCo_2O_4$ [16–23]. A microscopic understanding of the cation distribution, defects, local atomic coordination, electronic structure, as well as their influence on these properties is of vital importance for $NiCo_2O_4$ to be most effectively utilized in various applications.

Most of the previous works on $NiCo_2O_4$ have mainly centered on polycrystalline powders or mesoporous materials with poor control over cation distribution, valence states, defects, and impurities, which make it difficult to establish a definite structure-property relationship [17,24–26]. Note that the phase of $NiCo_2O_4$ becomes unstable in air at temperatures $>500\,^{\circ}C$ and transforms into a rock-salt structure at high temperature [27]. Therefore, stabilizing spinel $NiCo_2O_4$ requires material synthesis at low temperature, yet it limits the crystalline quality of synthesized material.

Recently, the growth of high-quality $NiCo_2O_4$ epitaxial thin films has been achieved using pulsed laser deposition (PLD) [7,14,15,22]. The electrical and magnetic properties of the grown films can be systematically controlled by growth temperature (T_G), i.e., films grown at lower temperature exhibit a ferrimagnetic metallic state, while those grown at higher temperature are nonmagnetic and insulating [3,15,28]. Moreover, the anomalous Hall effect persisting above room temperature (RT) has been recently observed in very thin $NiCo_2O_4$ epitaxial films, which was attributed to the electronic structure and correlation effects in Ni and Co $3d$ orbitals [7]. The high-quality epitaxial thin films open the opportunity to unravel the effect of cation distributions and local atomic structures on the electrical, optical, and magnetic properties. Moreover, knowledge regarding the electronic structure of $NiCo_2O_4$, e.g., the electronic density of states (DOS) at the Fermi level (E_F), the electronic origins for the metallic $NiCo_2O_4$, and the semiconducting $NiCo_2O_4$, remains quite limited. Such information on electronic structure is of crucial importance because it determines the optoelectronic properties and catalytic behavior for the reaction pathway in electrocatalysis.

Motivated by the growing interest in $NiCo_2O_4$ for various applications and to address fundamental questions, in this paper, we report a detailed study on the local atomic structure, electronic structure, and defect chemistry of epitaxial $NiCo_2O_4$ thin films and discuss the correlation against their optical, transport, and magnetic properties. We grew structurally well-defined $NiCo_2O_4$ epitaxial films with well-controlled electronic and magnetic properties on single-crystal $MgAl_2O_4$ (001) substrates using PLD. The cation distribution, valence state, and local coordination environments were examined by x-ray photoemission spectroscopy (XPS), x-ray absorption near edge structure (XANES), and extended x-ray absorption fine structure (EXAFS). A combination of resonant photoemission spectroscopy (resPES), x-ray absorption spectroscopy (XAS), and density functional theory (DFT) calculations were used to study the nature of the DOS at E_F. We demonstrated that the Ni^{3+} state promoted by low growth temperature introduces delocalized Ni $3d$-derived states at E_F, responsible for the metallic state in $NiCo_2O_4$, while the Co $3d$ state is more localized at high energy. In the semiconducting films where most of the Ni cations are at $+2$ oxidization state, the delocalized Ni $3d$ states disappear, and a gap state opens.

II. EXPERIMENTAL AND COMPUTATIONAL DETAILS

Epitaxial $NiCo_2O_4$ thin films were grown on double-sided polished (001)-oriented $MgAl_2O_4$ substrates by PLD. Laser ablation was performed at a repetition rate of 10 Hz and an energy density of 2.5 J/cm^2 with a 248 nm KrF excimer laser. Films with thicknesses of ~ 40 nm were grown

at different substrate temperatures from 325 to 525 °C. The oxygen partial pressure (pO_2) during growth was 50 mTorr, unless otherwise specified. The crystal structure and epitaxial relationship in the films was determined by high-resolution XRD using a PANalytical four-circle diffractometer in θ-2 θ scans and reciprocal space mapping (RSM) mode. Electrical resistivity measurements [Quantum Design Physical Property Measurement System (PPMS)] were performed using the van der Pauw method with Au contacts in the temperature range of 10–380 K. The surface morphologies were characterized by atomic force microscopy (AFM; Asylum Research MFP-3D-SA) in tapping mode. Optical absorption measurements were performed at RT using a Cary 5000 spectrophotometer in the photon energy range of 0.45–5.0 eV. Macroscopic magnetic measurements were performed by using a Quantum Design MPMS SQUID-VSM magnetometer.

XPS measurement using a laboratory monochromatic Al Kα_1 x-ray ($h\nu = 1486.6$ eV) source was carried out at normal emission (electron takeoff angle = 90° relative to the surface plane) with a SPECS PHOIBOS 150 electron energy analyzer. The total energy resolution was ~0.50 eV. The binding energy (BE) was calibrated by an Au foil in electrical contact with $NiCo_2O_4$ thin films, which simultaneously helped to avoid charging effects during XPS measurements. Soft XPS and XAS measurements were performed at the Soft X-ray (SXR) beamline, Australian Synchrotron. The XAS measurements at the O K edge and Co and Ni L edges were measured by a retarding grid analyzer using linearly polarized x rays in partial electron-yield mode with an energy resolution of 200 meV. The resPES were recorded by a SPECS Phoibos 150 Hemispherical Analyzer at normal emission with a p-polarized beam at a grazing incidence angle of 7 ° and an electron energy resolution of 150 meV. The BE scale was calibrated with respect to E_F measured from Au 4f from Au foils measured in parallel with the data. The intensities of the ResPES spectra were normalized to scan time and incident photon flux. These measurements were done in ultrahigh vacuum, i.e., $<10^{-10}$ mTorr. Hard x-ray photoelectron spectroscopy (HAXPES) measurements were performed using a 5.93 keV photon energy at the I09 beamline of the Diamond Light Source (DLS). HAXPES spectra were energy-resolved and measured using a VG Scienta EW4000 high-energy analyzer with a 56 ° acceptance angle. XAS measurements at the Co and Ni K edges were conducted at the CLAESS beamline, ALBA synchrotron (Spain) using a Si (311) monochromator with an incident energy resolution of 0.3 eV. Harmonics rejection was achieved by choosing proper angle and coating of a collimating and focusing mirror. The XAS spectra were recorded in fluorescence mode at RT. Co and Ni foils were used as reference samples and for energy calibration, which were measured in transmission mode. XANES and EXAFS data were processed with the ATHENA software package.

DFT plus Hubbard U correction ($U = 3.5$ eV for Ni ions and 5.5 eV for Co ions) calculations were carried out using the projector augmented-wave method, as implemented in the Vienna *Ab initio* Simulation Package (VASP) [29,30]. Projector augmented-wave pseudopotentials were used to describe the interaction between ions and electrons; the exchange-correlation potential was described by the generalized gradient approximation with the Perdew-Burke-Ernzerhof parameterization. The optimization calculations were performed with a 4 × 4 × 4 k-points sampling and a cutoff energy of 500 eV. The convergence criteria for total energies and forces were 10^{-4} eV and 0.02 eV/Å. The structure models of perfect $NiCo_2O_4$ were constructed by the special quasirandom structure approach [31,32]. To investigate the influence of oxygen vacancies, we considered two defective $NiCo_2O_4$ with different vacancy concentrations (9.375 and 18.75%), the optimized geometric structures are shown in Fig. S12 in the Supplemental Material [33]. Based on the $NiCo_2O_4$ cubic supercell, including 56 atoms and 32 oxygen atoms, we constructed the structures of defective $NiCo_2O_4$ with vacancy concentrations of 9.375 and 18.75% by introducing 3 and 6 oxygen vacancies, respectively. To avoid the interaction between two oxygen vacancies, the positions of oxygen vacancies were chosen to be at (0.364, 0.366, 0.862), (0.886, 0.884, 0.388), and (0.386, 0.114, 0.117) for 9.375% V_O-$NiCo_2O_4$ and (0.364, 0.366, 0.862), (0.886, 0.884, 0.388), (0.386, 0.114, 0.117), (0.864, 0.636, 0.633), (0.864, 0.136, 0.133), and (0.364, 0.866, 0.362) for 18.75% V_O-$NiCo_2O_4$.

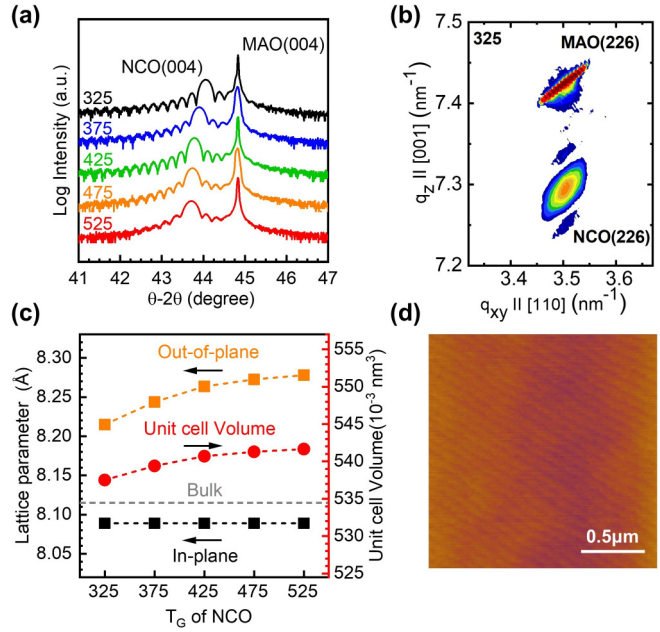

FIG. 2. (a) X-ray diffraction (XRD) θ-2θ scans around the (004) reflections of the $NiCo_2O_4$ films grown at different T_G in 50 mTorr oxygen partial pressure (pO_2). (b) Reciprocal space maps (RSMs) around the $MgAl_2O_4$ (226) reflections for the 325 °C grown film. (c) Changes of the lattice parameters and unit cell volumes as a function of T_G. (d) Atomic force microscopy (AFM) image of the 375 °C grown film, in which the atomic steps and atomic terrace with average width of 100 nm can be observed.

III. RESULTS AND DISCUSSION

A. Epitaxial thin film growth and crystalline structure

Bulk spinel $NiCo_2O_4$ has a lattice parameter of $a_{NiCo_2O_4} = 8.116$ Å. High-quality thin films can be epitaxially grown on $MgAl_2O_4$ ($a_{MgAl_2O_4} = 8.083$ Å) substrates with a small compressive lattice mismatch of ~0.4%. Figure 2(a) shows

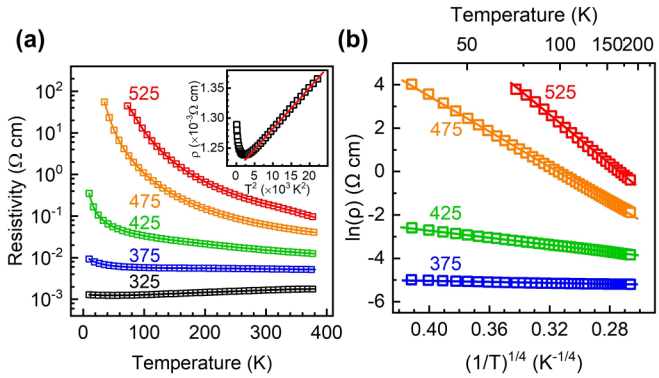

FIG. 3. (a) Temperature-dependent resistivity for $NiCo_2O_4$ films grown at different T_G. The inset shows resistivity vs T^2 in the temperature range of 65–150 K for the metallic film. (b) Fittings of the $\rho-T$ with variable range hopping model for the semiconducting films from 200 to 35 K.

the XRD θ-2θ out-of-plane scans of the epitaxial films grown at different T_G. The $NiCo_2O_4$ (004) peak region shows well-defined Kiessig fringes, confirming the high crystalline quality and planar character of the surfaces and interfaces of the epitaxial films. To gain additional structural information, RSMs near the (226) reflection of $MgAl_2O_4$ were measured and are shown in Figs. 2(b) and S1 in the Supplemental Material [33]. The in-plane and out-of-plane lattice parameters of the films were extracted from RSMs and are shown in Fig. 2(c). The in-plane lattice parameters are nearly the same as that of $MgAl_2O_4$, indicating the films are coherently strained by the substrates. However, the out-of-plane lattice parameters of the epitaxial films are slightly larger than the bulk value, which may be caused by the compressive in-plane strain that leads to an increase in the out-of-plane lattice parameter [34]. Furthermore, the out-of-plane lattice parameters also increase from 8.21 to 8.28 Å as the growth temperature increases. This is caused by larger ionic radius and longer bonding length of O_h Ni^{2+} cations than those of O_h Ni^{3+} and/or formation of oxygen vacancies promoted at higher growth temperature, as evidenced by XPS and XAS discussed in the following sections. Typical AFM images shown in Figs. 2(d) and S2 in the Supplemental Material [33] further confirm the atomically uniform films over a large lateral scale.

B. Carrier transport properties

The growth temperature dramatically impacts the electrical and magnetic properties of the films. Figure 3(a) shows the temperature-dependent electrical resistivity ($\rho-T$). The films grown at 325 °C exhibit a metallic conduction behavior with a RT ρ of 1.6×10^{-3} Ω cm. Upon decreasing the measurement temperature, the ρ decreases to 1.2×10^{-3} Ω cm down to 45 K and then shows an upturn <45 K [inset in Fig. 3(a)]. As shown in Fig. S3(a) in the Supplemental Material [33], the resistivity of metallic film shows T-linear dependence >150 K, indicating a normal electron-photon coupling as the main carrier scattering mechanism, but deviations from linearity are observed in the temperature range of 65–150 K. In this region, the resistivity fits well with $\rho = \rho_0 + AT^2$ [Fig. 3(a) inset], with $\rho_0 = 1.2 \times 10^{-3}\Omega$ cm and $A = 6.9 \times 10^{-9}$ Ω cm K^{-2}. The T^2 dependence of resistivity reflects the existence of Fermi-liquid-like electron-electron scattering in the metallic $NiCo_2O_4$, which was commonly observed in strongly correlated $3d$ perovskite oxides such as $LaNiO_3$, $SrVO_3$, and $SrCrO_3$ [35,36]. A slight upturn behavior is observed at temperature <45 K, which is likely induced by localization of charge carriers due to cation disorder or defects. In contrast, the films grown at $T_G > 375$ °C show clear semiconducting behavior, i.e., increase of resistivity with decreasing of temperature due to carriers frozen. The RT resistivities range from 5.4×10^{-3} Ω cm for films grown at 375 °C to 1.9×10^{-1} Ω cm at 525 °C (see Table I). To understand the conduction mechanism in the semiconducting films, we fit the ρ-T relations using a small polaron hopping (SPH) model [$\rho \propto T \exp(E_a/kT)$] and a band conduction model [$\rho \propto \exp(E_a/kT)$] in the temperature range of 200–380 K. As shown in Fig. S4 in the Supplemental Material [33] and Table I, the ρ-T relations fit slightly better with the band conduction model. Similarly, authors of a recent terahertz spectroscopic study have also suggested the bandlike conduction in $NiCo_2O_4$ [3]. The determined E_a increases from 2.5 to 69.7 meV for the band conduction model and from 26.3 to 93.4 meV for the SPH model. At temperatures <200 K, the ρ-T relations fit well with a variable-range hopping (VRH) model [$\rho \propto \exp(T_0/T)^{1/4}$] [Fig. 3(b)], suggesting the localization of charge carriers at low temperatures [37]. The T_0 in the model is the characteristic temperature associated with the density of the localized states at E_F, and the dramatic change of T_0 (Table I) suggests that charge carriers are much more localized for the high-T_G films [38,39].

C. Determination of oxidization state and local atomic coordination

High-resolution XPS and XAS were used to probe the oxidization states and local electronic structures of Co and Ni cations in the films. The Ni $2p$ and Co $2p$ XPS spectra in Fig. 4(a) show complex lineshapes by virtue of multiplet splitting, satellite, and mixed oxidization states. The multiplet splitting in transition metal (TM) $2p$ XPS spectra results from the interaction of a photonionized core hole with the unpaired electrons in the out-shell $3d$ orbitals. Therefore, the lineshape of the multiplet splitting is sensitive to the oxidization state of TM and can be used to distinguish different oxidization states [40]. As shown in Fig. 4(a) (left panel), the Ni $2p_{3/2}$ XPS spectra consist of the main line at BE of ~854 eV (marked as "A") and shoulder ("B") at ~856 eV resulting from multiplet splitting, and the satellite structure ("Sat.") at 861 eV. It has been demonstrated that the intensity ratio of B/A can be used as an indicator for the oxidization state of Ni, i.e., a higher B/A ratio corresponds to more Ni^{3+} state [41]. Therefore, as shown in Fig. 4(a), we compare the Ni $2p_{3/2}$ with those of reference samples: NiO of mainly Ni^{2+} oxidization state and $Li_{0.32}Ni_{0.78}O$ with half of the Ni at the Ni^{3+} state. The Ni $2p_{3/2}$ for the 525 °C grown films is like that of Ni^{2+} in NiO, while more Ni^{3+} state appears for low T_G films. This trend is further supported by the Ni L-edge XAS shown in Fig. 4(b) (left panel). The Ni L-edge XAS for higher T_G films exhibit a narrower L_3 edge and more pronounced double peak feature at the L_2 edge, characteristic of the Ni^{2+} state, while

TABLE I. Fitting parameters for band conduction, SPH, and VRH models.

T_G (°C)	ρ at RT ($\times 10^{-3}$ Ω cm)	E_a for band conduction model (meV)	E_a for SPH model (meV)	T_0 for VRH model (K)	R^2 for band conduction model	R^2 for SPH model	R^2 for VRH model
375	5.37	2.5	26.3	1.4	0.95418	0.99073	0.96249
425	15.3	20.2	43.9	4.9×10^3	0.99202	0.99258	0.99883
475	61.1	48.3	72.0	2.6×10^6	0.99940	0.99807	0.99984
525	193.5	69.7	93.4	1.0×10^7	0.99343	0.99351	0.99951

much more broadened peaks at both L_3 and L_2 edges are observed in the metallic films grown at low T_G, reflecting the existence of Ni^{3+} state.

We then discuss the electronic features of the Co element, which is more complicated than the Ni element in $NiCo_2O_4$ because, in addition to the multiplet splitting and mixed valences of Co^{2+} and Co^{3+}, Co cations spatially occupy both T_d and O_h sites. For Co^{3+} at O_h sites, there should be no appreciable multiplet splitting because of the low-spin configuration of Co^{3+} ($3d\ t_{2g}^6 e_g^0$) with zero unpaired electrons [40,42]. This behavior is proved by the Co $2p$ spectrum from $ZnCo_2O_4$ in which the Co $2p_{3/2}$ only shows the main peak with narrow width. Therefore, the broad feature in the energy region from 780 to 783 eV in the Co $2p_{3/2}$ spectra should be associated with Co at T_d sites with +2 or +3 oxidization states, where multiplet splitting occurs due to the unpaired $3d$ electrons, leading to the broader and asymmetric lineshape, which is like that of Co_3O_4. Nonetheless, putting all the Co $2p$ spectra together, there is no appreciable change of lineshapes for the different T_G films. Furthermore, the Co L-edge XAS [right panel in Fig. 4(b)] for $NiCo_2O_4$ films grown at $T_G < 425$ °C also exhibit a similar spectral shape, suggesting there is not much change of the oxidization state of Co as the T_G increases. However, for the 525 °C grown film, a small pre-edge feature appears at ~772.2 eV, characteristic of O_h-coordinated Co^{2+} [43,44]. This may be associated with the formation of a CoO secondary phase, as will be discussed later.

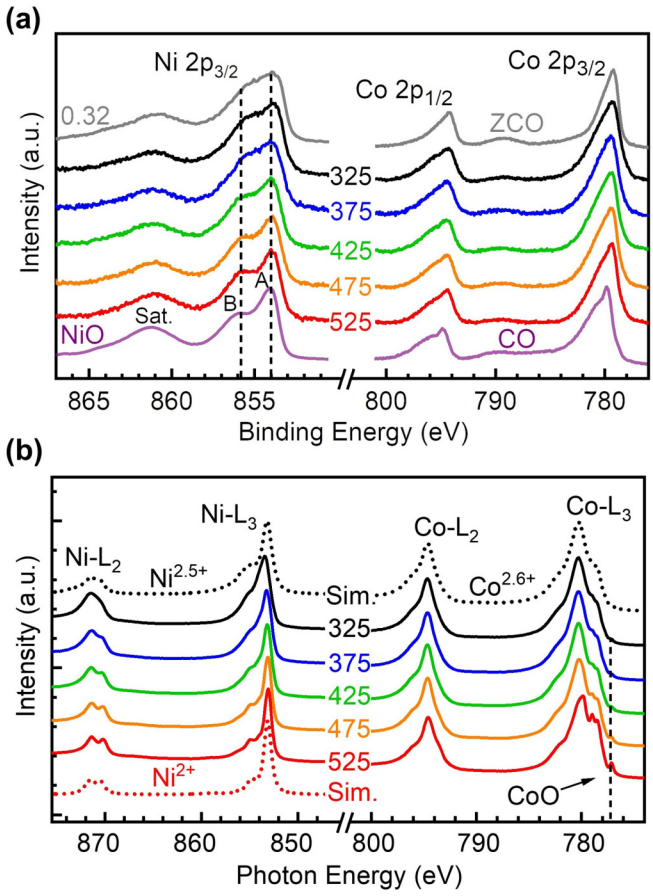

FIG. 4. (a) X-ray photoemission spectroscopy (XPS) core level spectra of Ni $2p_{3/2}$ (left) and Co $2p$ (right) along with reference spectra of NiO representing Ni^{2+}, $Li_{0.32}Ni_{0.68}O$ (denoted as 0.32) representing $Ni^{2.5+}$, $ZnCo_2O_4$ (ZCO) representing Co^{3+} in O_h symmetry, and Co_3O_4 (CO) representing a mixture of Co^{3+} and Co^{2+}. (b) Ni L-edge (left) and Co L-edge x-ray absorption spectroscopy (XAS; right) spectra, along with CI simulated XAS (dashed) for Ni^{2+} in NiO, $Ni^{2.5+}$ by linear combination of simulated spectra of NiO and $LiNiO_2$, and $Co^{2.6+}$ by linear combination of simulated spectra of $ZnCo_2O_4$ and $CoAl_2O_4$.

We further carried out configuration interaction (CI) cluster calculations to simulate the Ni and Co L-edge XAS spectra of the $NiCo_2O_4$ thin films. The Ni L-edge XAS from NiO (NiO_6 cluster with $3d^8$ configuration) and $LiNiO_2$ (NiO_6 cluster with $3d^7$ configuration) and the Co L-edge XAS from $ZnCo_2O_4$ (CoO_6 cluster with $3d^6$ configuration) and $CoAl_2O_4$ (CoO_4 cluster with $3d^7$ configuration) were also simulated as references [42,45]. The calculated spectra shown in Figs. 4(b) (dashed lines) and S5 in the Supplemental Material [33] were obtained with optimized parameters that can reproduce the experimental spectra well. The obtained parameters are shown in Table II. Detailed comparison of the experimental and the simulated XAS suggests that the average oxidization state of Ni is +2.5 in the 325 °C film, and +2 in the 525 °C film. The average oxidization state of Co is +2.6 and generally remains the same for all the films.

The oxidization states and local atomic coordination of Ni and Co are also measured by Ni and Co K-edge XANES and

TABLE II. Optimized parameters including the crystal field splitting energy ($10Dq$), charge transfer energy (Δ), hybridization energy ($pd\sigma$), Coulomb interaction (U_{dd}), and the attractive interaction between the core hole and the $3d$ electron (U_{pd}) for Co and Ni with different electronic configurations.

	$10Dq$ (eV)	Δ (eV)	$pd\sigma$ (eV)	U_{dd} (eV)	U_{pd} (eV)
Ni^{3+} $3d^7$	2	0.5	1	7	8
Ni^{2+} $3d^8$	0.56	4.7	1.2	7.3	8.5
Co^{2+} $3d^7$	0.8	4	0.5	2	2.6
Co^{3+} $3d^6$	0.8	3	0.5	2	2.6

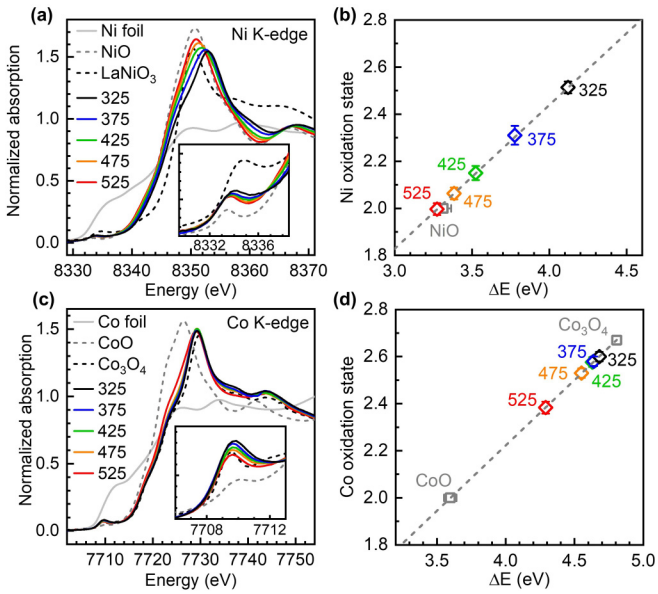

FIG. 5. X-ray absorption near edge structure (XANES) spectra at the (a) Ni K edge and (c) Co K edge from $NiCo_2O_4$ films grown at different T_G along with reference spectra. Insets show the zoom-in region of $1s-3d$ pre-edge. The calibration curves for the oxidation states of (b) Ni and (d) Co as a function of energy shift (ΔE) obtained by the integral method.

EXAFS spectra. Figure 5(a) shows the Ni K-edge XANES, showing that the onsite of absorption for low-T_G thin films is shifted by 0.86 eV toward higher energy than films grown at higher T_G films, indicating the increase of the Ni valence state in low-T_G films. The dipole-forbidden $1s$-$3d$ pre-edge peak also shows a similar shift by 0.5 eV toward higher energy. On the other hand, the Co K-edge XANES and pre-edge peak only show very small shift toward higher energy for low-T_G films, suggesting only a slight increase in the Co oxidization states [Fig. 5(c)]. We used the procedure by Capehart *et al.* [46] to quantitatively determine the oxidization states of the Ni and Co. Details on the procedure are described in Fig. S6 in the Supplemental Material [33]. Figures 5(b) and 5(d) show the calibration curves for the oxidation state vs energy shift values (ΔE). It was determined that the average oxidization state of Ni is +2 in the 525 °C grown film and gradually increases to be +2.54 in the 325 °C film, i.e., suggesting around half of the Ni cations are at the Ni^{3+} state. On the other hand, the Co oxidization state only shows a slight increase from +2.4 to +2.6. The determined oxidization state by XANES quantitatively agrees well with the above XPS and soft XAS results.

Figure 6 shows phase-corrected Fourier transform (FT) $k^2\chi(k)$ for the Co and Ni K-edge EXAFS, which provides detailed information on the local atomic structure. The FT-EXAFS for spinel oxide exhibits three distinct peaks [see Fig. 6(a)]: the first peak (marked as "I") at ~1.9 Å corresponds with the TM-O scatterings for both metal cations at the T_d and O_h sites, the second peak II at ~3 Å is attributed to the cation-cation bond between two O_h sites, and the third feature III at ~3.4 Å corresponds with the scatterings involving cations in T_d sites (between two T_d sites or between one

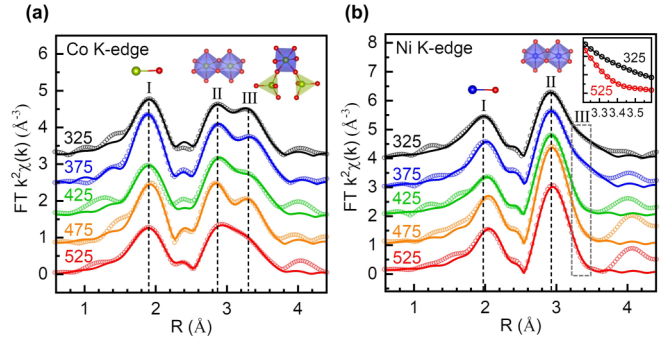

FIG. 6. Phase shift corrected Fourier transform (FT) $k^2\chi(k)$ spectra (circles) and fitting results (solid lines) at (a) Co K edge and (b) Ni K-edge. Inset shows the comparison of the peak III region for films grown at 325 and 525 °C.

at the T_d site and one at the O_h site) [26,47–49]. As shown in Fig. 6(a), all the Co K-edge FT-EXAFS for the films grown at different T_G exhibit a similar Co-O bond distance of ~1.92 Å (see Table S1 in the Supplemental Material [33]), peak II at ~3 Å, and prominent peak III at ~3.5 Å, indicating the presence of Co at both T_d and O_h sites. At the Ni K edge shown in Fig. 6(b), the first peak is attributed to the Ni_{Oh}-O bond. For the 525 °C grown film, the Ni-O bond length was determined to be 2.08 Å (Table S2 in the Supplemental Material [33]), characteristic of Ni^{2+}, while the Ni-O bond length was determined to be 1.98 Å for the 325 °C grown film, suggesting the presence of more Ni^{3+} state [24]. The Ni K-edge FT-EXAFS for high-T_G films shows a prominent peak ~3 Å but no appreciable feature at 3.4 Å, which implies that Ni is overwhelmingly in O_h coordination. However, for the 325 °C grown film, a very small shoulder gradually grows at 3.4 Å (peak III), indicating a small portion of Ni cations may occupy the T_d sites. Authors of a recent polarized Raman study have also observed mixed cation distribution at T_d and O_h sites for the low temperature grown films [19]. However, the amount of Ni at the T_d site should be quite small as judged by the intensity of peak III.

D. Electronic structures near the Fermi level

We further used XPS valence band (VB) and O K-edge XAS spectra to investigate the occupied and unoccupied DOS near E_F. Figure 7(a) shows the XPS VB spectra measured with photon energies of 1486.6 eV and 5930 eV, providing the occupied DOS weighted by the photoionization cross-sections of the contributing orbitals. All the VB spectra are referenced to E_F as zero. Overall, all the films show similar VB spectra. According to the electronic configuration (Fig. 1) and following DFT calculations, region I in the VB spectra at BE of 0–4 eV is mainly derived from the occupied Co and Ni $3d$ orbitals, and region II at 4–10 eV is mainly from O $2p^6$ orbitals with certain hybridization with Ni/Co $3d$ states. A clear DOS is observed across E_F in the energy range of −0.4 to 0.4 eV for 325 and 375 °C grown films, suggestive of a metallic state. On the other hand, for the high-T_G films, the VB maximum (VBM) moves away from E_F, and negligible DOS remains at E_F, thereby driving the film toward a semiconducting state. As shown in Fig. S7 in the Supplemental Material

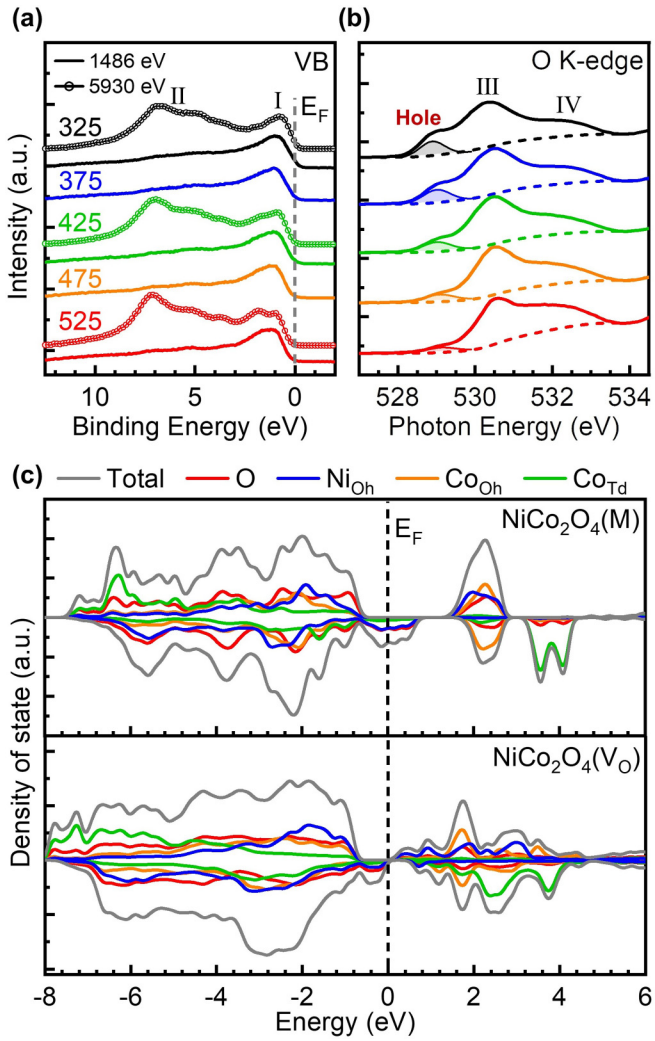

FIG. 7. (a) Valence band spectra of $NiCo_2O_4$ grown at different T_G excited with photon energies of 1486 eV (solid lines) and 5930 eV (line + circles). (b) O K-edge x-ray absorption spectroscopy (XAS) spectra of $NiCo_2O_4$ grown at different T_G. (c) Calculated projected density of states (PDOS) for metallic $NiCo_2O_4$ (up) and $NiCo_2O_4$ with 18.75% oxygen vacancies (V_O; down).

[33], the shift of VBM away from E_F is also in parallel with the increase in RT resistivity with T_G. Interestingly, we also observed that the spectral intensity of region II for these films is significantly enhanced when measured using 5930 eV photon energy compared with measuring by 1486.6 eV, which suggests the contribution of Co 4s and Ni 4s orbitals to these states because of the relatively enhanced cross-sections for s orbitals at higher photon energy [50,51].

Figure 7(b) shows O K-edge XAS spectra of the thin films. O K-edge XAS probes the electronic transitions from the O 1s core level to unoccupied states with a partial O 2p character hybridized with Ni and Co 3d orbitals and thus can be qualitatively related to unoccupied DOS [52]. The O K-edge absorption spectra shown in Fig. 7(b) can be discussed in three regions: region III at photon energy of 530–531 eV, region IV at 531–534 eV, and the "hole state" at 528–530 eV. Comparing with our previous results [42,53] and DFT calculations [Fig. 7(c)], we inferred that the feature in region III is attributed to the unoccupied Co 3d states and the shoulder in region IV to the empty e_g states of Ni^{2+}. The hole state at 529 eV increases with the decrease of T_G. Based on the above results that there are more Ni^{3+} states in the low-T_G films and Co stays at the same oxidization state, we can conclude that the hole state should be associated with an unoccupied e_g orbital of Ni^{3+} and/or hole state at O 2p because of the enhanced O 2p-Ni 3d hybridization induced by the high-valent Ni^{3+}. The hole state progressively grows and merges with the occupied DOS at the top of VB, leading to a semiconductor-to-metal transition in low-T_G $NiCo_2O_4$ films.

To gain further understanding of the XPS VB and O K-edge XAS spectra, we used the DFT + U method to calculate the electronic structure of metallic $NiCo_2O_4$. The U values chosen for Ni and Co atoms were 3.5 and 5.5 eV, respectively. The calculated projected DOS (PDOS) in the upper panel of Fig. 7(c) [marked as $NiCo_2O_4$(M)] shows good agreement with the experimental VB and O K-edge XAS spectra of the metallic $NiCo_2O_4$ (325 °C). The calculated PDOS shows both the occupied and unoccupied states at the energy region from −1 to 1 eV around E_F mainly derived from the e_g orbitals of Ni 3d with certain hybridization with O 2p, in agreement with the VB and O K-edge XAS spectra. The occupied DOS at the energy region from −8 to −1 eV originates from the hybridized states of Ni 3d, Co 3d, and O 2p, in accordance with region II in VB. The unoccupied DOS at 2 and 4 eV, which are associated with unoccupied orbitals of Co 3d and Ni 3d, also agree with features III and IV in O K-edge XAS spectra.

E. ResPES to determine the nature of electronic states at E_F

The above XPS VB spectra indicate that the appearance of occupied DOS at E_F leads to the metallic state in $NiCo_2O_4$. ResPES were performed to further elucidate the character of the occupied DOS at E_F. Tuning the photon energies near the Ni 2p-3d or Co 2p-3d absorption edges, resonant enhancement in the photoemission intensity occurs due to the interference between the direct ($2p^63d^n + h\nu \rightarrow 2p^63d^{n-1} + e^-$) and indirect ($2p^63d^n + h\nu \rightarrow 2p^53d^{n+1} \rightarrow 2p^63d^{n-1} + e^-$) processes [54,55]. The specific element enhanced VB spectra can be used to distinguish the respective contribution of Ni 3d or Co 3d to the VB. Figure S8 in the Supplemental Material [33] shows the VB spectra of 325 °C grown film (metallic) and 475 °C film (semiconducting) excited with a series of photon energies around the Ni 2p-3d and Co 2p-3d resonances, respectively. The excitation energies are marked on the Ni and Co L_3-edge XAS spectra shown in Figs. S8(a) and S8(d) in the Supplemental Material [33]. The VB spectra show considerable enhancement at both Ni and Co L_3-edge absorption energies, thus indicating both Ni 3d and Co 3d states spread over a wide range of VB because of their strong hybridization with O 2p orbitals. We are interested in the evolution of spectra features around E_F. For the 325 °C grown film, Fig. 8(a) shows that the spectral intensity at 0.3 eV (marked as "A") is significantly enhanced at the Ni 2p-3d resonant energy (∼853.3 eV). However, the intensity enhancement around E_F is much smaller at the Co 2p-3d resonant energy (∼780 eV), see Fig. 8(c). On the other hand, there is a significant enhance-

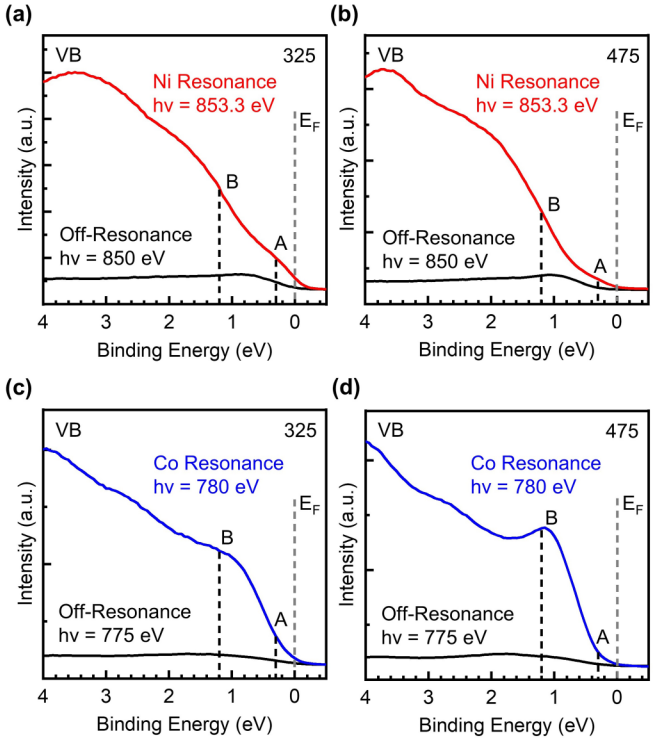

FIG. 8. Valence band spectra of the (a) 325 °C metallic and (b) 475 °C semiconducting $NiCo_2O_4$ films excited with photon energies corresponding to the Ni 2*p*-3*d* resonance and off-resonance conditions. Valence band spectra of the (c) 325 °C and (d) 475 °C $NiCo_2O_4$ films excited with photon energies corresponding to the Co 2*p*-3*d* resonance and off-resonance conditions.

ment for the 1.2 eV BE feature (B) at the Co 2*p*-3*d* resonant energy, indicating most of the Co 3*d* states are much more localized than the Ni^{3+} states. This comparison indicates the electronic state associated with Ni^{3+} 3*d* ($t_{2g}^6 e_g^1$) is the main origin for the itinerant metallic state at E_F. This is further supported by VB spectra at the Ni 2*p*-3*d* resonant energy for the semiconducting film shown in Fig. 8(b), in which the spectral intensity at E_F is tiny. However, there is still some degree of intensity enhancement of feature A related to Ni 3*d*, probably due to the localized electronic state associated with the remaining Ni^{3+} state, but its concentration is too low to give rise to a metallic state. Furthermore, the intensity enhancement around E_F at the Co 2*p*-3*d* resonant energy is still negligible for the semiconducting film [Fig. 8(d)]. This is consistent with the above results that there is only a slight change of the oxidization state for Co for different T_G films. The Ni e_g state at E_F is in agreement with theoretical results based on DFT + *U* calculations that the DOS at E_F of $NiCo_2O_4$ consists of spin-down e_g electrons of the O_h coordinated Ni^{3+} ($t_{2g}^6 e_g^1$), leading to a half-metallic electronic state. Lowering the oxidization state of Ni to +2 leads to considerable decrease of the DOS at E_F and reduction of the hole state at the CB, likely arising from the strong electron correlation effect in the 3*d* orbitals of Ni^{2+} ($t_{2g}^6 e_g^2$) [41]. This effect can be exemplified by NiO, which has a large band gap of 3.65 eV due the strong electron correlation effect, whereas $LaNiO_3$ shows a metallic state because of the half-occupied e_g orbital [35,41,56,57].

F. Discussion on defect chemistry and implication for optoelectronic applications

Our local atomic and electronic structure characterizations and DFT calculations highlight the Ni 3*d*-related electronic state at E_F is the key factor in determining the electrical transport properties of $NiCo_2O_4$ films. For higher T_G films, most of the Ni are at the Ni^{2+} oxidization state. A negligibly small amount of the DOS is observed at E_F, and the films exhibit semiconducting behavior with a small band gap. On the other hand, low growth temperature stabilizes the Ni^{3+} oxidization state, which introduces delocalized electronic states at E_F and is responsible for the metallic state in lower T_G films. Detailed analysis on XAS suggests that around half of the Ni cations are at a +3 oxidization state for the 325 °C grown films. However, the Co-related electronic states do not contribute much to the transport properties of $NiCo_2O_4$, as the electronic states associated with Co 3*d* are more localized to energies away from E_F, and the Co oxidization state only slightly increases from +2.4 in high-T_G films to +2.6 in low-T_G films. The semiconductor-to-metal transition driven by Ni^{3+}-induced electronic structure in $NiCo_2O_4$ is quite like the hole-doping-induced insulator-to-metal transition occurring in many other TM oxides, such as Sr-doped $LaMnO_3$, $LaCrO_3$, and $LaCoO_3$ [52,58,59]. For $NiCo_2O_4$ with an inverse spinel structure, most of the Ni cations are at the O_h sites with edge sharing with other octahedra but corner sharing with other tetrahedra (see Fig. 1). The O_h chains in the structure are most likely the carrier conduction channels in metallic $NiCo_2O_4$ because of the more effective orbital overlap in edge-sharing octahedra for delocalizing electrons. Furthermore, as demonstrated by the magnetic measurements shown in Fig. S9 in the Supplemental Material [33], the metallic behavior in low-T_G films also accompanies appearance of a ferrimagnetic state, highlighting the crucial role of Ni^{3+} for triggering the magnetic property in $NiCo_2O_4$. The interesting coexistence of the metallic behavior and ferrimagnetism implies that the double exchange (DE) interactions among the mixed-valent $Ni^{3+/2+}$ and T_d-site $Co^{3+/2+}$ bridged by oxygen might be responsible for stabilizing the magnetic ordering in $NiCo_2O_4$. Indeed, authors of recent x-ray magnetic circular dichroism studies have demonstrated that the spin magnetic moments in the metallic $NiCo_2O_4$ films dominantly originate from the T_d-site Co and the O_h-site Ni, while the O_h-site Co shows little contribution because of the zero spin state of Co $3d^6$ ($t_{2g}^6 e_g^0$) [44]. Our detailed spectroscopic results provide microscopic insight into the electronic structure associated with Ni oxidization states for the electrical and magnetic properties of $NiCo_2O_4$.

$NiCo_2O_4$ is also a useful electrode material for photovoltaics and flat panel display applications because of its high *p*-type conductivity and reasonable transparency in the infrared light spectrum region [4,5,28]. It is interesting to discuss the optical properties of $NiCo_2O_4$ films based on the present study on the electronic structure. Figure 9(a) shows the optical absorption spectra of the $NiCo_2O_4$ films grown at different > T_G. For the high-T_G films, three distinct absorption

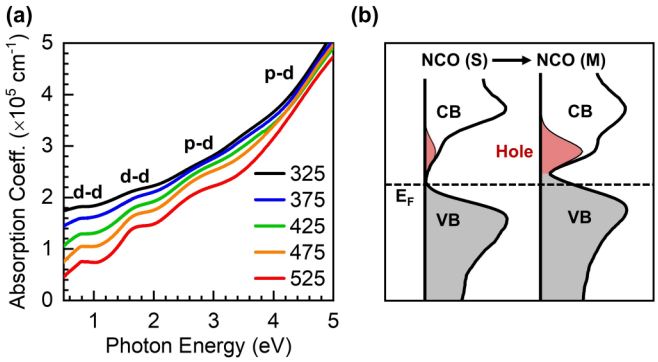

FIG. 9. (a) Optical absorption coefficients of the $NiCo_2O_4$ films as a function of photon energy. (b) Detailed comparison of measured occupied density of states (DOS) [valence band (VB)] and unoccupied DOS [conduction band (CB)] near E_F for the semiconducting [NCO(S)] and metallic [NCO(M)] films.

bands centered at ∼0.8, ∼1.7, and ∼2.6 eV can be observed in the infrared-visible light region. Based on the absorption band centered at ∼0.8 eV, together with experimentally measured VB and O K-edge XAS, we can estimate that the band gap of the semiconducting $NiCo_2O_4$ should be some value <0.8 eV. According to the electronic configuration and the VB and O K-edge XAS spectra, the absorption bands centered at ∼0.8 eV may originate excitations from e to t_2 of T_d-site Co, while the ones at ∼1.7 and ∼2.6 eV may originate from t_{2g}-to-e_g transitions of O_h-site Co. The energy for excitation of the Ni^{2+} state at the O_h site should be much larger in the ultraviolet region, considering the 3.65 eV band gap of NiO [57]. Therefore, the optical excitations in $NiCo_2O_4$ in the infrared-visible region are quite like that of Co_3O_4 (see Fig. S10 in the Supplemental Material [33]). Using combined x-ray spectroscopic characterizations and DFT calculations, we have determined that Co_3O_4 has a fundamental band gap of ∼0.8 eV, ∼1 eV less than the generally accepted values [42]. The band gap arises from the excitation at the T_d-site Co^{2+} cations. Although this d-d transition would be nominally forbidden according to the dipole selection rule, the hybridization of Co 3d with O 2p orbitals will slightly relax the parity selection rule and result in weak light absorption. This could explain the reasonable transparency of $NiCo_2O_4$ film in the visible and infrared region despite its small band gap. It should be noted that our determined band gap value of the semiconducting $NiCo_2O_4$ is also much smaller than the reported values of 2.58, 1.6, and 1.1 eV determined merely by optical absorption measurement [28,60]. We believe our comprehensive combination of optical measurement with XPS VB, O K-edge XAS, and DFT calculations provides a more accurate description of the nature of the band gap of $NiCo_2O_4$. For the low-T_G metallic films, the absorption coefficient in the infrared light region increases. This is attributed to the optical excitation from the states at the top of the VB to the emergent hole state associated with Ni^{3+} [Fig. 9(b)].

Lastly, one important question that remains open is how the growth temperature drives the change of the Ni oxidization state and the semiconductor-to-metal transition in $NiCo_2O_4$. We propose that the formation of oxygen vacancies (V_O) and/or the rock-salt secondary phase at high growth temperature are the possible origin for the Ni^{2+} oxidization state, as discussed below. First, our quantitative analysis of the XPS, Co and Ni L-edge XAS, and K-edge XANES data shows that the average oxidization state of Ni cations decreases from +2.54 to +2.06 when T_G increases from 325 to 475 °C. Somehow unexpectedly, the Co oxidization state also slightly decreases from +2.6 to +2.52 over the same T_G range. However, based on the Co and Ni K-edge XANES and the FT fitting of the EXAFS in Figs. 5 and 6, there is only a small amount of site redistribution between Ni and Co cations. Therefore, formation of V_O seems to be a possible way to maintain charge neutrality in the high temperature grown films, i.e., $Ni^{2+}Co_2^{+2.5}O_{4(1-\delta)}$. By valence electron counting, δ is 0.03 for the 325 °C metallic film and 0.11 for the 475 °C semiconducting film. The tendency to form V_O has been observed in many Ni^{3+}-based oxides such as $LaNiO_3$ and $NdNiO_3$ and causes the materials to change from a metallic state into a semiconducting state [61,62]. To further test this point, we also grew $NiCo_2O_4$ film under pO_2 of 300 mTorr with T_G = 325, 375, 425, and 475 °C. As shown in Table III and Fig. S11 in the Supplemental Material [33], all the films grown at 300 mTorr oxygen have lower resistivity, e.g., the 375 °C film turns into a metallic temperature-dependent transport property. We also carried out DFT + U calculations to find the DOS of $NiCo_2O_4$ with different concentrations of V_O. The calculated DOS for defected $NiCo_2O_4$ are shown in Fig. S13 in the Supplemental Material [33] and the lower panel of Fig. 7(c). With an increasing V_O concentration, the Ni 3d-related state at E_F gradually disappears, leading to the opening of a small band gap of ∼0.5 eV when V_O concertation δ reaches ∼18%, in agreement with the observed metal-to-semiconductor transition in the $NiCo_2O_4$ films grown at different T_G. Our results also suggest that V_O mostly change the electronic states of Ni, while leaving the Co states nearly unchanged. This is in line with the calculation by Shi *et al.* [21] that V_O at sites coordinated to Ni^{3+} cations have a smaller formation energy. Furthermore, our XAS characterization [Fig. 4(b)] indicates the formation of CoO secondary phases at T_G of 525 °C. Recently, Sharona *et al.* [63] using high-resolution transmission electron microscopy observed the formation of a nanosized (3–7 nm) rock-salt $Ni_{1-y}Co_yO$ phase in $NiCo_2O_4$ films grown in the same conditions as ours. The tendency to form a secondary rock-salt phase is in line with the low thermodynamic stability

TABLE III. RT resistivity of $NiCo_2O_4$ films grown under 50 and 300 mTorr with different T_G.

	325 °C	375 °C	425 °C	475 °C
50 mTorr	1.6×10^{-3} Ω cm	5.4×10^{-3} Ω cm	1.5×10^{-2} Ω cm	6.1×10^{-2} Ω cm
300 mTorr	1.2×10^{-3} Ω cm	2.0×10^{-3} Ω cm	8.2×10^{-3} Ω cm	2.3×10^{-2} Ω cm

of $NiCo_2O_4$. $NiCo_2O_4$ was reported to become unstable after annealing at 600 °C in vacuum and to decompose into mixed Ni-Co oxide films [19]. It is also interesting to note that the formation of a rock-salt phase is in line with the formation of V_O. The chemical formula would turn into $(NiCo_2)O_3$ when the V_O concentration reached $\delta = 0.25$ (as an extreme case). Here, $(NiCo_2)O_3$ could be viewed as the solid solution of NiO and CoO with a ratio of 1:2. Both rock-salt NiO and CoO are antiferromagnetic and insulating [64,65] and would have important influence on the transport and magnetic properties of $NiCo_2O_4$, especially at the low-temperature region.

IV. CONCLUSIONS

In this paper, we have performed a detailed investigation on the local cation distribution, electronic structure, and defect chemistry of epitaxial $NiCo_2O_4$ thin films and their correlation with electrical, optical, and magnetic properties. Our combined x-ray spectroscopic characterization and theoretical calculations clearly demonstrate the crucial role of the Ni 3*d*-related electronic state at E_F in determining the electronic and optical properties of $NiCo_2O_4$ films. We showed that the Ni^{3+} state stabilized at low growth temperature introduces delocalized Ni 3*d*-derived states at E_F, responsible for the metallic state. However, for higher temperature grown films, the valence state of Ni is lowered and $\sim +2$, and the delocalized Ni 3*d*-derived electronic states at E_F disappear, and a band gap opens, leading to a semiconducting state due to the strong electron correlation effect in 3*d* orbitals of Ni^{2+}. It should be noted that the Co-related electronic states do not contribute much to the transport properties of $NiCo_2O_4$, as the electronic states associated with Co 3*d* are more localized to energies away from E_F. Further structural and defect chemistry study indicates that the oxygen vacancies and secondary CoO phases at high growth temperature cause the formation of a Ni^{2+} valence state in $NiCo_2O_4$. The band gap of the semiconducting $NiCo_2O_4$ is estimated to be <0.8 eV, which is much smaller than the quoted values in the literature. Despite the small band gap, its optical transition is mostly *d*-*d* dipole forbidden, and therefore, the semiconducting $NiCo_2O_4$ still shows reasonable transparency in the infrared-visible light region. The high *p*-type conductivity and reasonable transparency make $NiCo_2O_4$ a desirable *p*-type transparent semiconductor for various optoelectronic applications. The present results advance our fundamental understanding and provide significant guidance for the use of $NiCo_2O_4$ in electrocatalysis, opto-electronics, and spintronics.

ACKNOWLEDGMENTS

K.H.L.Z. is grateful for funding support by the National Natural Science Foundation of China (NSFC; Grants No. 21872116 and No. 22075232). J.C. gratefully acknowledges the financial support by the NSFC (Grants No. 21621091 and No. 21373166). K.H.L.Z. and J.C. gratefully acknowledge funding from the State Key Laboratory of Physical Chemistry of Solid Surfaces for the "single-crystal electrochemistry" project. L.Q. acknowledges the support by the NSFC (Grants No. 11774044 and No. 52072059). L.-S.W. acknowledges the support by the NSFC (Grant No. 51771157). D.-C.Q. acknowledges the support of the Australian Research Council (Grant No. FT160100207) and the continued support from the Queensland University of Technology (QUT) through the Centre for Materials Science. F.E.O. and V.A.d.l.P. are grateful for funding support by the EU (ERC CoG HyMAP 648319) and Spanish MINECO (PID2019-106315RB-I00). V.A.d.l.P. also wishes to thank "Comunidad de Madrid" and European Structural Funds for their financial support of the FotoArt-CM project (S2018/NMT-4367) and the Fundación Ramón Areces. Part of this research was undertaken on the Soft X-ray Spectroscopy beamline at the Australian Synchrotron, part of ANSTO. We also thank beamline scientist Dr. Bruce Cowie at the Australian Synchrotron for his kind assistance. Part of this research was carried out in the BL22-CLAESS beamline at the ALBA Synchrotron radiation source.

[1] Q. Zhao, Z. Yan, C. Chen, and J. Chen, Chem. Rev. **117**, 10121 (2017).
[2] W.-W. Li, J. Shi, K. H. L. Zhang, and J. L. MacManus-Driscoll, Mater. Horiz. **7**, 2832 (2020).
[3] P. Silwal, C. La-o-vorakiat, E. E. M. Chia, D. H. Kim, and D. Talbayev, AIP Adv. **3**, 092116 (2013).
[4] C. F. Windisch, G. J. Exarhos, K. F. Ferris, M. H. Engelhard, and D. C. Stewart, Thin Solid Films **398**, 45 (2001).
[5] A. Zakutayev, T. R. Paudel, P. F. Ndione, J. D. Perkins, S. Lany, A. Zunger, and D. S. Ginley, Phys. Rev. B **85**, 085204 (2012).
[6] K. Zhang, C. Zhen, W. Wei, W. Guo, G. Tang, L. Ma, D. Hou, and X. Wu, RSC Adv. **7**, 36026 (2017).
[7] X. Chen, X. Zhang, M. G. Han, L. Zhang, Y. Zhu, X. Xu, and X. Hong, Adv. Mater. **31**, 1805260 (2019).
[8] D. P. Dubal, P. Gomez-Romero, B. R. Sankapal, and R. Holze, Nano Energy **11**, 377 (2015).
[9] Y. Li, P. Hasin, and Y. Wu, Adv. Mater. **22**, 1926 (2010).
[10] Q. Wang, B. Liu, X. Wang, S. Ran, L. Wang, D. Chen, and G. Shen, J. Mater. Chem. **22**, 21647 (2012).
[11] M. Wang, X. Sui, Y. Wang, Y. Juan, Y. Lyu, H. Peng, T. Huang, S. Shen, C. Guo, J. Zhang, Z. Li, H. Li, N. Lu, A. T. N'Diaye, E. Arenholz, S. Zhou, Q. He, W. Duan Y. Chu, and P. Yu, Adv. Mater. **31**, 1900458 (2019).
[12] L. Hu, L. Wu, M. Liao, and X. Fang, Adv. Mater. **23**, 1988 (2011).
[13] X. Shi, S. L. Bernasek, and A. Selloni, J. Phys. Chem. C **121**, 3929 (2017).
[14] Y. Shen, D. Kan, Z. Tan, Y. Wakabayashi, and Y. Shimakawa, Phys. Rev. B **101**, 094412 (2020).
[15] P. Silwal, L. Miao, I. Stern, X. Zhou, J. Hu, and D. Ho Kim, Appl. Phys. Lett. **100**, 032102 (2012).
[16] J. F. Marco, J. R. Gancedo, M. Gracia, J. L. Gautier, E. I. Ríos, H. M. Palmer, C. Greaves, and F. J. Berry, J. Mater. Chem. **11**, 3087 (2001).

[17] P. D. Battle, A. K. Cheetham, and J. B. Goodenough, Mater. Res. Bull. **14**, 1013 (1979).

[18] M. Xue, X. Chen, S. Ding, Z. Liang, Y. Peng, X. Li, L. Zha, W. Yang, J. Han, S. Liu, H. Du, C. Wang, and J. Yang, ACS Appl. Electron. Mater. **2**, 3964 (2020).

[19] M. N. Iliev, P. Silwal, B. Loukya, R. Datta, D. H. Kim, N. D. Todorov, N. Pachauri, and A. Gupta, J. Appl. Phys. **114**, 033514 (2013).

[20] P. F. Ndione, Y. Shi, V. Stevanovic, S. Lany, A. Zakutayev, P. A. Parilla, J. D. Perkins, J. J. Berry, D. S. Ginley, and M. F. Toney, Adv. Funct. Mater. **24**, 610 (2014).

[21] X. Shi, S. L. Bernasek, and A. Selloni, J. Phys. Chem. C **120**, 14892 (2016).

[22] I. Suzuki, D. Kan, M. Kitamura, Y. Shen, K. Horiba, and Y. Shimakawa, J. Appl. Phys. **127**, 203903 (2020).

[23] A. Tsujie, Y. Hara, T. Yanase, T. Shimada, and T. Nagahama, Appl. Phys. Lett. **116**, 232404 (2020).

[24] J. F. Marco, J. R. Gancedo, M. Gracia, J. L. Gautier, E. Ríos, and F. J. Berry, J. Solid State Chem. **153**, 74 (2000).

[25] C. F. Windisch, K. F. Ferris, G. J. Exarhos, and S. K. Sharma, Thin Solid Films **420**, 89 (2002).

[26] D. Loche, C. Marras, D. Carta, M. F. Casula, G. Mountjoy, and A. Corrias, Phys. Chem. Chem. Phys. **19**, 16775 (2017).

[27] D. P. Lapham and A. C. C. Tseung, J. Mater. Sci. **39**, 251 (2004).

[28] Y. Bitla, Y. Chin, J. Lin, C. N. Van, R. Liu, Y. Zhu, H. Liu, Q. Zhan, H. Lin, C. Chen, Y. Chu, and Q. He, Sci. Rep. **5**, 15201 (2015).

[29] G. Kresse and J. Hafner, Phys. Rev. B **47**, 558 (1993).

[30] G. Kresse and J. Furthmüller, Phys. Rev. B **54**, 11169 (1996).

[31] A. Zunger, S. H. Wei, L. G. Ferreira, and J. E. Bernard, Phys. Rev. Lett. **65**, 353 (1990).

[32] L. Qiao, S. Zhang, H. Y. Xiao, D. J. Singh, K. H. L. Zhang, Z. J. Liu, X. T. Zu, and S. Li, J. Mater. Chem. C **6**, 1239 (2018).

[33] See Supplemental Material at http://link.aps.org/supplemental/10.1103/PhysRevB.104.125136 for additional RSMs, AFM images, fit of resistivity, XPS spectra, resPES spectra, optical absorption spectra, magnetic measurements, CI calculations, details regarding estimation of oxidation state from XANES, and results of EXAFS fitting.

[34] K. H. L. Zhang, A. Regoutz, R. G. Palgrave, D. J. Payne, R. G. Egdell, A. Walsh, S. P. Collins, D. Wermeille, and R. A. Cowley, Phys. Rev. B **84**, 233301 (2011).

[35] K. Sreedhar, J. M. Honig, M. Darwin, M. McElfresh, P. M. Shand, J. Xu, B. C. Crooker, and J. Spalek, Phys. Rev. B **46**, 6382 (1992).

[36] K. H. L. Zhang, Y. Du, P. V. Sushko, M. E. Bowden, V. Shutthanandan, L. Qiao, G. X. Cao, Z. Gai, S. Sallis, L. F. J. Piper, and S. A. Chambers, J. Phys.: Condens. Matter. **27**, 245605 (2015).

[37] P. H. Xiang, N. Zhong, C. G. Duan, X. D. Tang, Z. G. Hu, P. X. Yang, Z. Q. Zhu, and J. H. Chu, J. Appl. Phys. **114**, 243713 (2013).

[38] R. Scherwitzl, S. Gariglio, M. Gabay, P. Zubko, M. Gibert, and J. M. Triscone, Phys. Rev. Lett. **106**, 246403 (2011).

[39] C. Zhen, X. Zhang, W. Wei, W. Guo, A. Pant, X. Xu, J. Shen, L. Ma, and D. Hou, J. Phys. D: Appl. Phys. **51**, 145308 (2018).

[40] J. van Elp, J. L. Wieland, H. Eskes, P. Kuiper, G. A. Sawatzky, F. M. F. de Groot, and T. S. Turner, Phys. Rev. B **44**, 6090 (1991).

[41] J. Y. Zhang, W. W. Li, R. L. Z. Hoye, J. L. MacManus-Driscoll, M. Budde, O. Bierwagen, L. Wang, Y. Du, M. J. Wahila, L. F. J. Piper, T.-L. Lee, H. J. Edwards, V. R. Dhanak, and K. H. L. Zhang, J. Mater. Chem. C **6**, 2275 (2018).

[42] X. C. Huang, J. Y. Zhang, M. Wu, S. Zhang, H. Y. Xiao, W. Q. Han, T.-L. Lee, A. Tadich, D.-C. Qi, L. Qiao, L. Chen, and K. H. L. Zhang, Phys. Rev. B **100**, 115301 (2019).

[43] C. F. Chang, Z. Hu, Hua Wu, T. Burnus, N. Hollmann, M. Benomar, T. Lorenz, A. Tanaka, H.-J. Lin, H. H. Hsieh, C. T. Chen, and L. H. Tjeng, Phys. Rev. Lett. **102**, 116401 (2009).

[44] D. Kan, M. Mizumaki, M. Kitamura, Y. Kotani, Y. Shen, I. Suzuki, K. Horiba, and Y. Shimakawa, Phys. Rev. B **101**, 224434 (2020).

[45] M. W. Haverkort, M. Zwierzycki, and O. K. Andersen, Phys. Rev. B **85**, 165113 (2012).

[46] T. W. Capehart, J. F. Herbst, R. K. Mishra, and F. E. Pinkerton, Phys. Rev. B **52**, 7907 (1995).

[47] C. Huck-Iriart, L. Soler, A. Casanovas, C. Marini, J. Prat, J. Llorca, and C. Escudero, ACS Catal. **8**, 9625 10,(2018).

[48] J. Timoshenko and B. Roldan Cuenya, Chem. Rev. **121**, 882 (2021).

[49] C. M. B. Henderson, J. M. Charnock, and D. A. Plant, J. Phys.: Condens. Matter. **19**, 076214 (2007).

[50] D. W. Davies, A. Walsh, J. J. Mudd, C. F. McConville, A. Regoutz, J. M. Kahk, D. J. Payne, V. R. Dhanak, D. Hesp, K. Pussi, T. Lee, R. G. Egdell, and K. H. L. Zhang, J. Phys. Chem. C **123**, 1700 (2019).

[51] S. K. Panda, B. Pal, S. Mandal, M. Gorgoi, S. Das, I. Sarkar, W. Drube, W. Sun, I. Di Marco, A. Lindblad, P. Thunström, A. Delin, O. Karis, Y. O. Kvashnin, M. van Schilfgaarde, O. Eriksson, and D. D. Sarma, Phys. Rev. B **93**, 235138 (2016).

[52] K. H. L. Zhang, Y. Du, P. V. Sushko, M. E. Bowden, V. Shutthanandan, S. Sallis, L. F. J. Piper, and S. A. Chambers, Phy. Rev. B **91**, 155129 (2015).

[53] M. Cui, X. Ding, X. Huang, Z. Shen, T.-L. Lee, F. E. Oropeza, J. P. Hofmann, E. J. M. Hensen, and K. H. L. Zhang, Chem. Mater. **31**, 7618 (2019).

[54] O. Tjernberg, S. Soderholm, U. O. Karlsson, G. Chiaia, M. Qvarford, H. Nylen, and I. I. Lindau, Phys. Rev. B **53**, 10372 (1996).

[55] H. Xu, R. Wu, J. Zhang, W. Han, L. Chen, X. Liang, C. Y. Haw, P. Mazzolini, O. Bierwagen, D.-C. Qi, and K. H. L. Zhang, ACS Appl. Electron. Mater. **3**, 1834 (2021).

[56] G. A. Sawatzky and J. W. Allen, Phys. Rev. Lett. **53**, 2339 (1984).

[57] K. H. L. Zhang, R. Wu, F. Tang, W. Li, F. E. Oropeza, L. Qiao, V. K. Lazarov, Y. Du, D. J. Payne, J. L. MacManus-Driscoll, and M. G. Blamire, ACS Appl. Mater. Interfaces **9**, 26549 (2017).

[58] M. Abbate, F. M. F. de Groot, J. C. Fuggle, A. Fujimori, O. Strebel, F. Lopez, M. Domke, G. Kaindl, G. A. Sawatzky, M. Takano, Y. Takeda, H. Eisaki, and S. Uchida, Phys. Rev. B **46**, 4511 (1992).

[59] A. Chainani, M. Mathew, and D. D. Sarma, Phys. Rev. B **46**, 9976 (1992).

[60] K. Dileep, B. Loukya, P. Silwal, A. Gupta, and R. Datta, J. Phys. D: Appl. Phys. **47**, 405001 (2014).

[61] M. Abbate, G. Zampieri, F. Prado, A. Caneiro, J. M. Gonzalez-Calbet, and M. Vallet-Regi, Phys. Rev. B **65**, 155101 (2002).
[62] L. Wang, S. Dash, L. Chang, L. You, Y. Feng, X. He, K. Jin, Y. Zhou, H. G. Ong, P. Ren, S. Wang, L. Chen, and J. Wang, ACS Appl. Mater. Interfaces **8**, 9769 (2016).
[63] H. Sharona, B. Loukya, U. Bhat, R. Sahu, B. Vishal, P. Silwal, A. Gupta, and R. Datta, J. Appl. Phys. **122**, 225301 (2017).
[64] T. Ambrose and C. L. Chien, Phys. Rev. Lett. **76**, 1743 (1996).
[65] M. Grimsditch, L. E. McNeil, and D. J. Lockwood, Phys. Rev. B **58**, 14462 (1998).